REGULAR PAPER

Studies on Structural, Dielectric, and Optical Properties of the Lanthanum Modified BF-BNT Perovskite for the Thermistor and Photovoltaic Applications

S. K. Parida[1]

Abstract

The modified structure of BF-BNT $(Bi_{0.5}La_{0.5}Fe)_{0.25}(Bi_{0.5}Na_{0.5}Ti)_{0.75}O_3)$ single perovskite is prepared by a conventional solid-state reaction technique. The structural analysis suggests a tetragonal crystal with space group P4bm (JCPDS file No. 01-070-4760). The average crystallite and lattice strains are 87.2 nm and 0.116% respectively. The dielectric study predicts negative temperature coefficient of resistance character while the presence of low dielectric loss makes the materials useful for energy storage devices. The analysis of the modulus study suggests the presence of a non-Debye type of relaxation process while a thermally activated relaxation process is confirmed from the study of ac conductivity. The presence of the depressed semicircular arcs in both Nyquist and Cole–Cole plots confirms the semiconductor nature of the sample. The study of the Raman spectrum confirms the presence of all atomic vibrations. The UV visible study provides the energy bandgap of 1.67 eV, suitable for the different optoelectronic devices.

Keywords $(Bi_{0.5}La_{0.5}Fe)_{0.25}(Bi_{0.5}Na_{0.5}Ti)_{0.75}O_3$ · Lattice strain · Non-Debye relaxation · Nyquist plots · Raman spectrum · Optoelectronic

1 Introduction

In the last few decades, there has been much interest in the field of ferroelectric materials due to their enormous applications in electronic devices such as a transducer, actuators, IR detectors and imaging, multilayer capacitors, modulators, ferroelectric random-access memory, and display, etc. [1–4]. The co-existence of different multiferroic properties in a single-phase material brings huge differences in terms of design and applications [5–7]. Particularly, magnetoelectric coupling plays an important role in manufacturing units. Now, people pay more attention to multiferroic materials because of the potential applications in the field of microelectronic devices and spintronics [8–10]. The most versatile multiferroic perovskite material is $BiFeO_3$; which has both ferromagnetic and ferroelectric properties [11]. It has been found from the literature that $BiFeO_3$ has ferroelectric

ordering below the temperature of 1103 K and antiferromagnetic ordering below the temperature of 643 K [12]. The presence of Fe^{3+} ions in d^5-electronic configuration in the B-site cations provides the magnetic phase and effective local magnetic moments that increased up to 5.9 μ_B [13]. The presence of the Bi^{3+} ions and six lone pairs of electrons in the A-site cations creates ferroelectricity in the distorted $BiFeO_3$ perovskite [14]. The study of the $BiFeO_3$ thin films grown epitaxially exhibits a large ferroelectric at 90 K which is mainly attributed to the effect of substrate, lattice strain, etc. [15]. On the other hand, the study of the $BiFeO_3$ ceramics and thin films provides enhanced dielectric, magnetic properties while producing low bandgap energy, for better photovoltaic applications [16, 17]

Sharma et al. [18] have studied the physical properties of $BiFeO_3$ ceramics by both solid-state reaction and sol–gel method. The structural analysis suggests that the formation of the phase is confirmed at high temperatures in the solid-state reaction method compared to sol–gel. The study of UV visible and M–H loop of the $BiFeO_3$ suggests a lower value energy bandgap and magnetization in solid-state reaction method compared to sol–gel. The material scientists have made many attempts to address the issues related to

✉ S. K. Parida
  santoshparida@soa.ac.in

1   Department of Physics, ITER, Siksha O Anusandhan Deemed to Be University, Bhubaneswar 751030, India

structural, dielectric, electrical, magnetic, and optical properties of the doped $BiFeO_3$ ceramics. Different synthesis techniques have been studied to look after the improvement of physical properties after doping different dopants concentrations in the host $BiFeO_3$ ceramics. The doping of the Nb and Nd in the pure $BiFeO_3$ provides the results in a decrease of bandgap energy and an increase of magnetization [19]. The addition of Eu^{+3} in the pure $BiFeO_3$ increases the dielectric constant and magnetic dipole moments [20]. However, the research of $BiFeO_3$ ceramics is limited due to some genuine problems like weak ferromagnetic order parameters and polarization. Again, the presence of the highly volatile bismuth and iron oxidation states may be the reason for leak current and weak ferroelectric nature [21–23].

It is remained a challenge to improve the physical properties of the perovskite for the material scientists, for which many permutations and combinations of different perovskite materials have been mixing with different proportions for the last few decades. The examples of some of the studied systems are BF–BF ($BiFeO_3$–$PrFeO_3$), BF–PT ($BiFeO_3$–$PbTiO_3$), BF–MT ($BiFeO_3$–$MgTiO_3$), BF–CT ($BiFeO_3$–$CaTiO_3$) etc. [24, 25]. Again, many people attempt to improve the physical properties of the $BiFeO_3$ by substituting suitable dopants; La^{3+}, Gd^{3+}, Mn^{4+}, Nb^{5+}, Pb^{2+}, Sr^{2+}, etc. [26]. So, research on the solid solution of the $BFO-ABX_3$ attracts material scientists to study the enhanced physical properties. The study of sodium-based perovskite plays an important role in the application of optoelectronic, microelectronic, and photovoltaics.

Presently, numerous synthesis techniques have been employed to prepare combined perovskite systems such as solid-state reaction methods, ball milling method, sol–gel method, and sintering in a spark discharge. Among all these methods, the high-temperature solid-state method is considered to be superior because of its advantages, including the particle shape, structure, composition, product homogeneity, and also low energy and cost. Keeping the above-mentioned points in mind and considering the potentiality of the BF compounds, we got motivated for the study of the physical properties of La-doped BF-BNT ceramic. We have synthesized La modified BF ceramics through the solid-state reaction method and reported the consistency of evolution of crystal structure, dielectric, electrical, and optical properties.

2 Experimental Detail

The solid-state reaction method is used to prepare the sample. The starting metal oxides and carbonate raw materials are Bi_2O_3, La_2O_3, Fe_2O_3, Na_2CO_3, and TiO_2. The materials are weighted stoichiometrically with the help of high accuracy balance up to 4th place of decimal. The mortar pestle is used to grind the metal powders for 2 h in dry medium and then 2 h in wet medium with the help of methanol. The fine powders were kept in a high-temperature resistant crucible in the furnace at 1100 °C for 10–12 h for calcination and XRD will confirm the formation of the sample. Then, the sample is sintered at 1150 °C for high densification and better homogeneity. The cylindrical pellets of diameter 10–12 mm and thickness 2 mm are made using powder sample in a hydraulic pressure with the help of 4 MPa pressure. Both sides of the pellets are painted with high conducting silver before connecting to the two ends of the electrical electrode for evaluation of the electrical reading. The Raman study provides the information of all constituent atomic vibrations in the sample. The UV visible study predicts the bandgap in the sample; which is suitable for different optoelectronic devices.

3 Results and Discussion

3.1 Sample Formation and XRD Analysis

The single perovskite ceramics is popularly known as ABO_3, where A-site is substituted by divalent elements and B-site is substituted by tetravalent elements. The tolerance factor of a single perovskite can be calculated by $t = \frac{r_A + r_o}{\sqrt{2}(r_B + r_0)}$, where r_A = ionic radius of A-atom, r_B = ionic radius of B-atom and r_0 = ionic radius of oxygen-atom. The conventional tolerance factor should lie within the range from 0.75 to 1.0 with additional condition; $r_A > 0.9$Å and $r_B > 0.51$Å nm [27, 28]. The ionic radii of Bi^{3+}, La^{3+} and Fe^{+3} is 1.04 Å, 1.06 Å and 0.78 Å respectively [29]. For calculation, $r_A = Bi_{0.5}La_{0.5}Fe = 0.5(1.04) + 0.5(1.06) + 0.78 = 1.83$ Å. Similarly, the ionic radii of Bi^{3+}, Na^{1+} and Ti^{+4} are 1.04 Å, 1.16 Å and 0.51 Å respectively, $r_B = Bi_{0.5}Na_{0.5}Ti = 0.5(1.04) + 0.5(1.16) + 0.605 = 1.61$ Å and $r_0 = 1.4$ Å. Therefore, tolerance factor of La doped bismuth ferrite single perovskite is 0.76, which is allowable range [30].

The XRD is an important tool to calibrate unknown, identification structure, space group, unit cell volume, and density. Figure 1a represents the XRD pattern of the $(Bi_{0.5}La_{0.5}Fe)_{0.25}(Bi_{0.5}Na_{0.5}Ti)_{0.75}O_3$ single perovskite. The presence of sharp and distinct intense peaks in the XRD pattern confirms the single-phase material. The X'Pert High-Score Plus software is used to analyze the structure of the sample. The XRD results confirm that sample has a tetragonal crystal structure with the P4bm space group (JCPDS file No. 01-070-4760). The refinement parameters of the sample are calculated with the simulation of different physical quantities including atomic position, the lattice constant, full width half maximum, shape parameter, scale factor, crystal orientation, and anisotropic temperature [31].
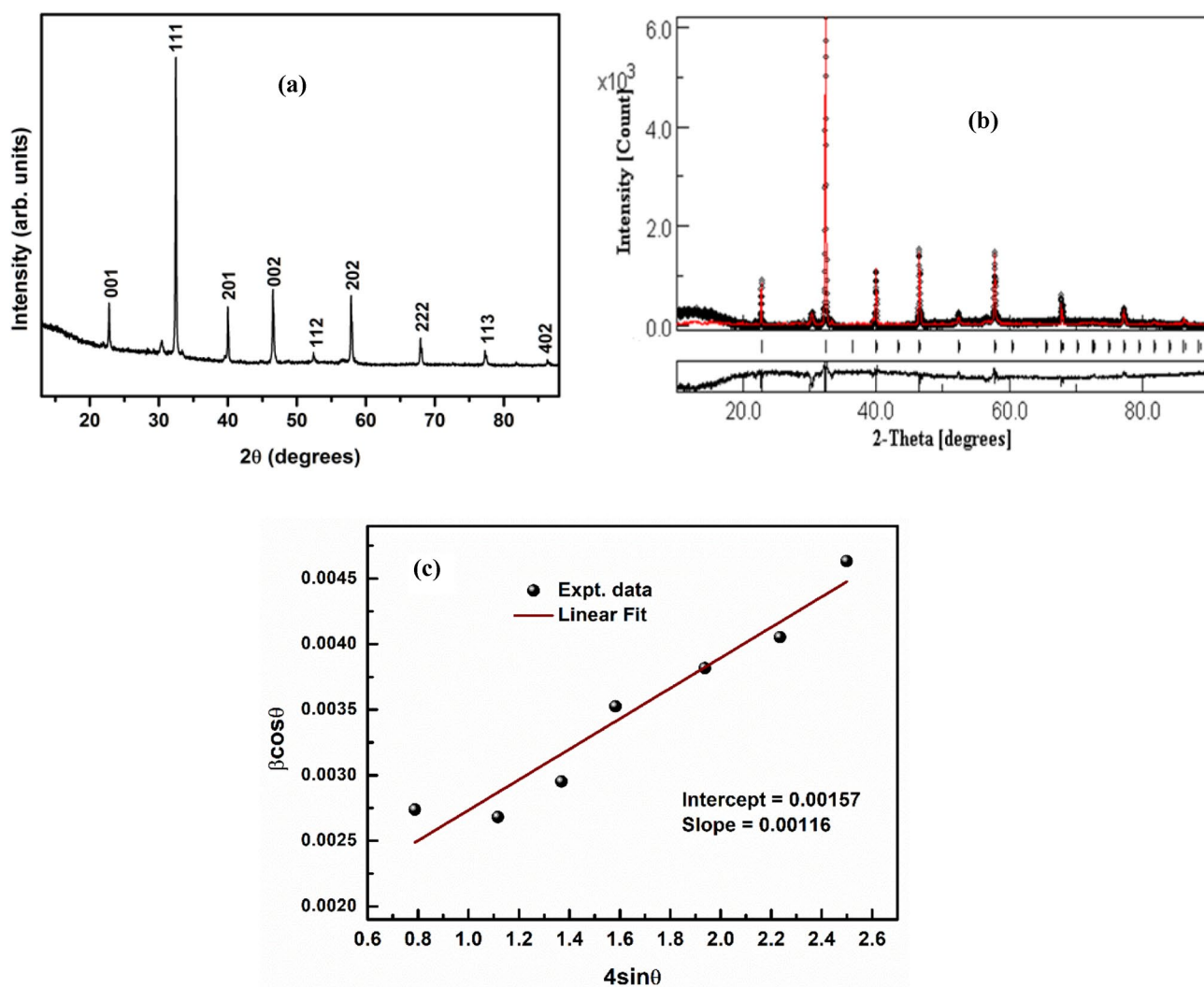
Fig. 1 **a** XRD pattern, **b** Rietveld refinement pattern, **c** Williamson–Hall plots

The calculated cell parameters are herewith given: $a = b = 5.519\text{Å}, c = 3.908\text{Å}, \alpha = 90^0, \beta = 90^0,$ and $\gamma = 90^0$. The volume and density of the unit cell of the sample are 119.1Å^3 and 5.91 g/cm^3 respectively. Figure 1b shows the Rietveld refinement of XRD data of the $(Bi_{0.5}La_{0.5}Fe)_{0.25}(Bi_{0.5}Na_{0.5}Ti)_{0.75}O_3$ single perovskite using Pseudo-Voigt function. The MAUD software is used to complete the Rietveld refinement analysis of the experimental XRD data of the prepared sample. The reliability factors obtained from the Rietveld refinement are the $R_{wp}(\%) = 19.04, R_{exp}(\%) = 5.29, R_B(\%) = 16.49,$ and $GOF = (chi)^2 = 3.62$ are well-matched with the previously reported modified BF-BNT compound. The quality of the Rietveld refinement is excellent because of the almost zero difference between experimental and computed data recorded. The crystal structure of the pure BiFeO$_3$ is rhombohedral with space group R3c, lattice constant

3.965 Å, and a rhombohedral angle $\alpha = 89.3^0$ to 89.4^0 at room temperature. The second host BNT has a cubic crystal structure with a space group (Pm$\bar{3}$m). After doping La in the bismuth site of the BiFeO$_3$, the modified structure of the sample is a tetragonal crystal structure (P4bm).

Figure 1c represents Williamson-Hall plots of the BF-BNT ceramics. The micro-lattice strain can be calculated by using a relation; $\beta\cos\theta = 4\varepsilon\sin\theta + k\lambda/D$, where k = 0.89, $\lambda = 0.154$ nm, D = average crystalline size, ε = lattice strain β = FWHM and θ = angle of diffraction. The intercept of the plot provides the average crystalline size, which is about 87.2 nm while the slope of the graph provides micro-lattice strain, which is about 0.116% [32].

The variation of dielectric constant and tan delta versus frequency is studied from Fig. 2a, b respectively. The observed disperse value of the dielectric constant at low
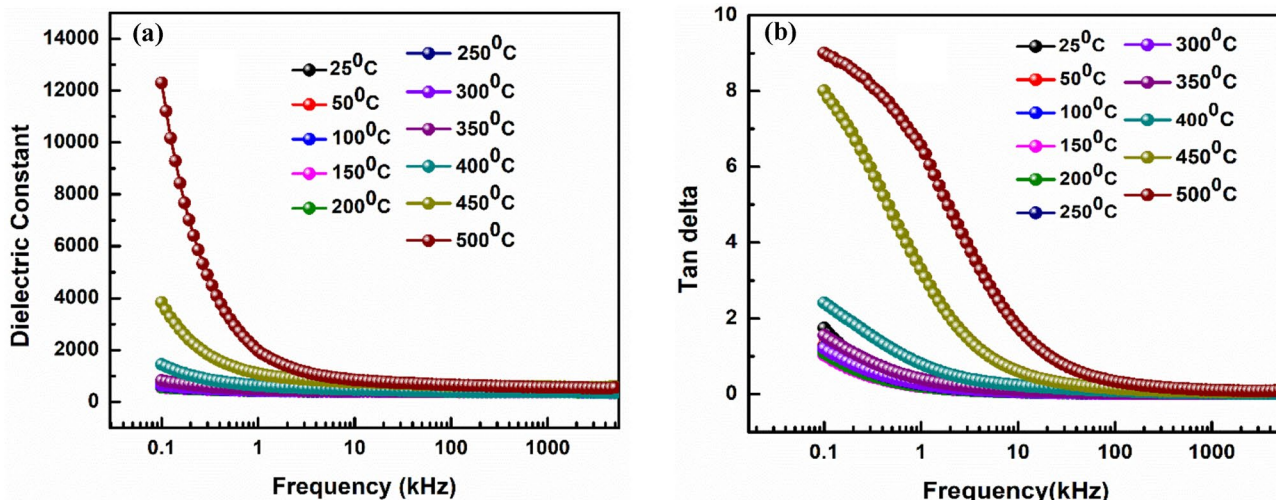
Fig. 2 **a** Dielectric versus frequency and **b** tan delta versus frequency

frequency is due to the presence of electronic, ionic, orientational, and space charge polarization. But, with an increase of frequency, the dielectric value decreases and merged at high frequency due to reduction of space charge polarization effect [33]. A similar observation is found in the tan delta versus frequency.

The effect of the temperature on both dielectric constant and tan delta is discussed in Fig. 3a, b respectively. At low temperature, the value of the dielectric constant is small and slowly increase with temperature. The value of the dielectric loss remains constant with the temperature at high frequency and slowly increases towards low frequency. Therefore, it may conclude that the sample is suitable to

work for microelectronic devices both at high frequency and temperature.

The role of the impedance to control the electrical properties of the sample is studied from Fig. 4a, b. The real part of the impedance decreases with the increase of temperature support the negative temperature coefficient of resistance (NTCR) behavior [34]. Similarly, the imaginary part of the impedance shows a wide disperse vale at low frequency. The frequency corresponding to maximum value of Z'' peaks is called relaxation frequency. Therefore, the sample has a relaxation character which is useful for sensor applications.

The semiconducting character of the sample is tested by using both Nyquist and Cole–Cole plots shown in Fig. 5a,
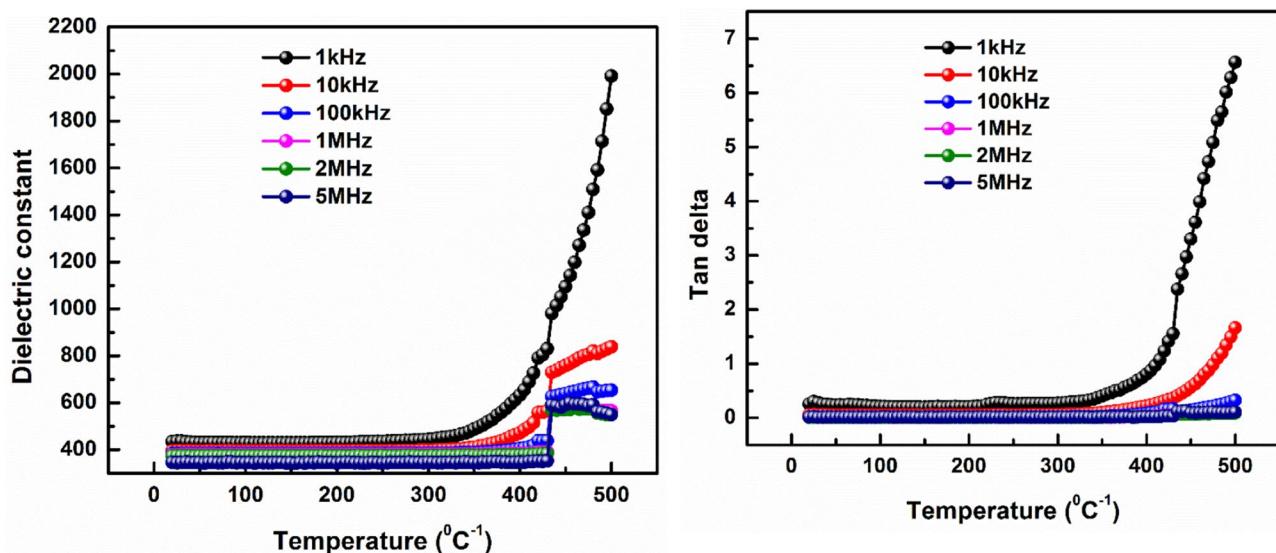

Fig. 3 **a** Dielectric constant versus temperature **b** tan delta versus temperature
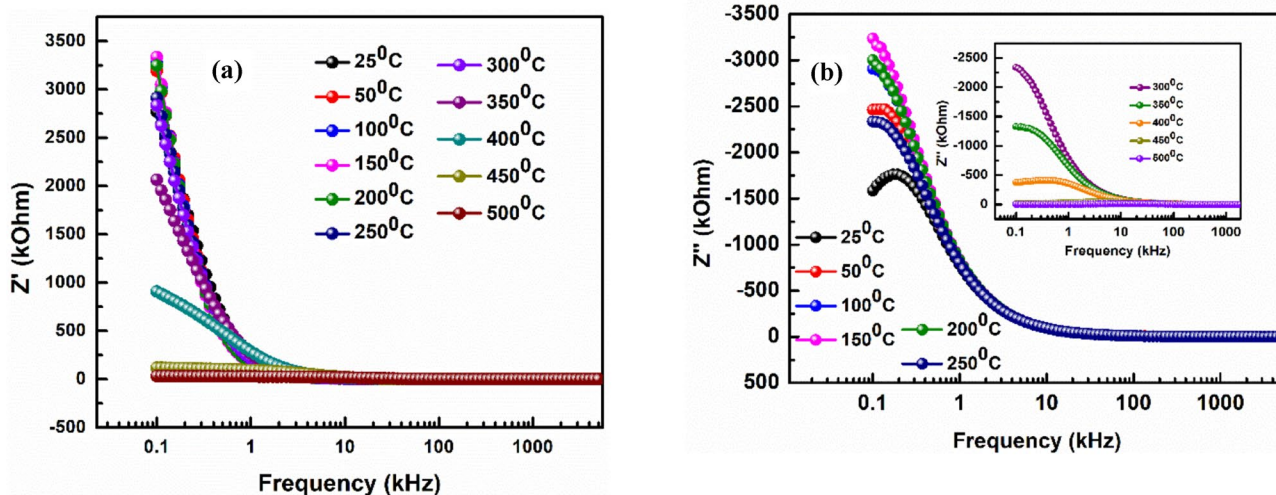
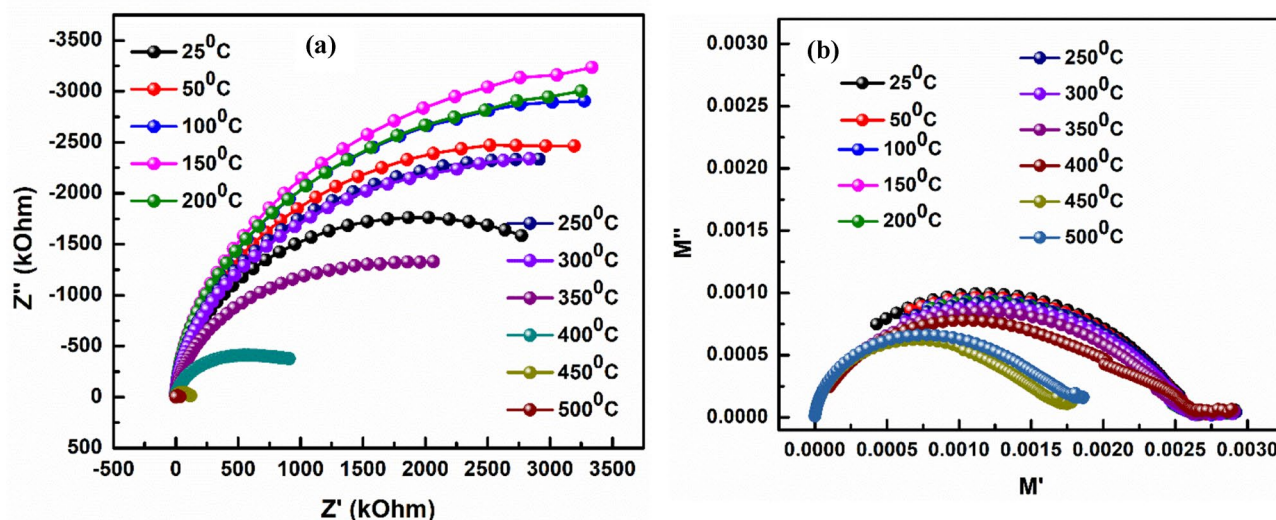Fig. 4 **a** Z′ versus frequency and **b** Z″ versus frequency

Fig. 5 **a** Nyquist plots and **b** Cole–Cole plots

b. The depressed semicircular arcs present in the Nyquist plots confirm the semiconductor behavior [35]. Similarly, the presence of perfect semicircular arcs supports the fact of semiconductor character and is well supported with Nyquist's results.

The non-Debye relaxation property of the sample is tested from the analysis of Fig. 6a, b. The two peaks of the Z″ and M″ intersect at some particular frequency. It is observed that the peaks are becoming wider with an increase of temperature; supporting the fact of the non-Debye type of relaxation process [36].

Figure 7a shows the variation of the M′ with frequency in a wide range of temperatures from 25 to 500 °C. It is observed that all the values of M′ are close to zero at low

frequency and slowly increase with both frequency and temperature. The plot of the M″ versus frequency is presented in Fig. 7b. It is observed that the peaks of the M″ are shifting with both frequency and temperature. The asymmetric peaks shift confirms the non-Debye type of the relaxation process [37].

The variation of the ac conductivity versus frequency and temperature was studied from Fig. 8a, b respectively. The value of the ac conductivity is maximum at low frequency for 500 °C and decreases with a decrease in temperature. Then, with an increase of frequency, the value of ac conductivity increases and merges into one. The calculated activation energies are 2.24 meV, 2.01 meV, 1.98 meV, 1.44 meV, 1.36 meV and 1.23 meV at 1 kHz, 10 kHz, 100 kHz, 1 MHz,
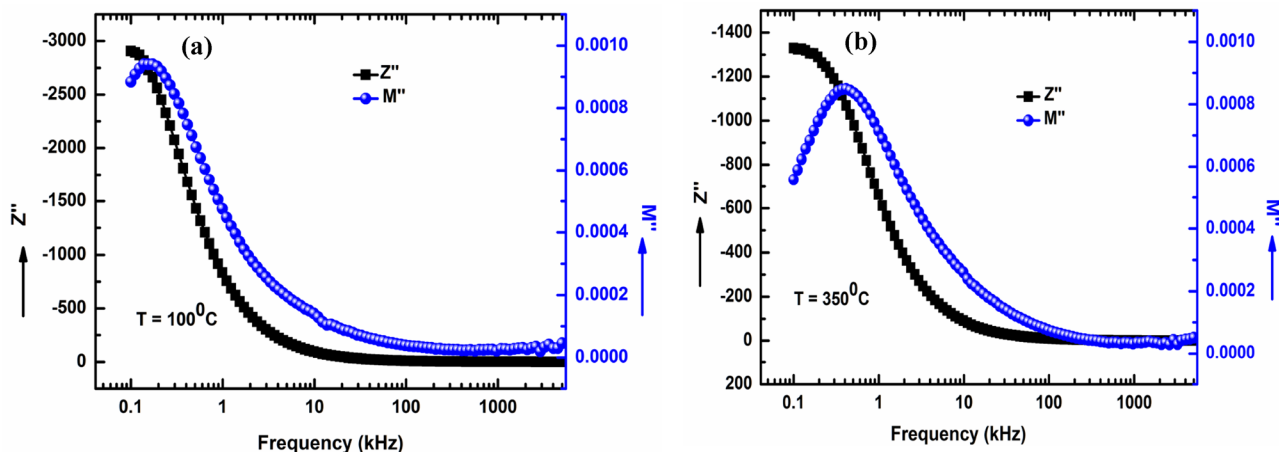
Fig. 6 **a** Z″ and M″ versus frequency at 100 °C and **b** Z″ and M″ versus frequency at 350 °C
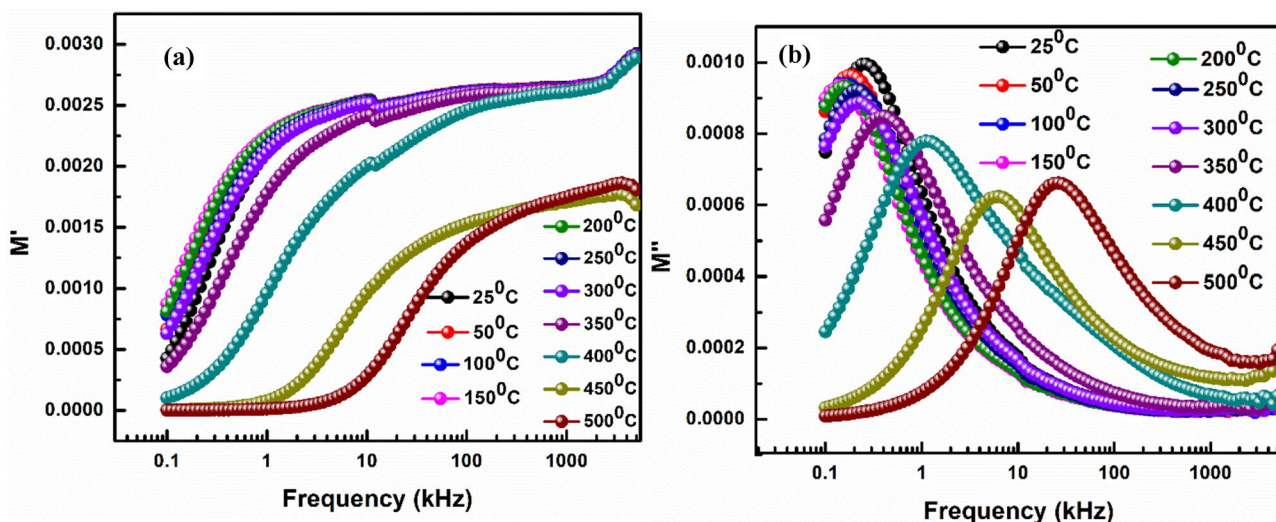

Fig. 7 **a** M′ versus frequency and **b** M″ versus frequency

2 MHz and 5 MHz respectively. The decreasing value of activation energy with an increase of frequency confirms the presence of a thermally activated relaxation process in the sample [38].

3.2 Resistance Versus Temperature

The variation of the resistance versus temperature is shown in Fig. 9a. It implies that resistance decreases with temperature, which confirms NTCR behavior and is also well supported by dielectric spectroscopy. If the resistance decreases with the increase of temperature in a thermistor, then it is called a negative temperature coefficient (NTC) thermistor. It has been used extensively because of highly sensitive to change of resistance and low cost [39]. In an NTC

thermistor, the relation between resistance and temperature can be written as; ln (R_T) = 1/T + C, where R_T = resistance at the corresponding temperature. The plot between lnR versus 1/T is shown in Fig. 9b, which confirms the NTC behavior of the thermistor.

3.3 Thermistor Constant (β)

The thermistor constant can be calculated from the resistance and temperature as; $\beta = ln\left(\frac{R_1}{R_2}\right)/\left(\frac{1}{T_1} - \frac{1}{T_2}\right)$, where all symbols have their usual meaning [40]. Here, in the present study, the NTC thermistor obeys Arrhenius's equation from the temperature 300–500 °C. Now, the resistance with thermistor constant can be written about NTC thermistor as;
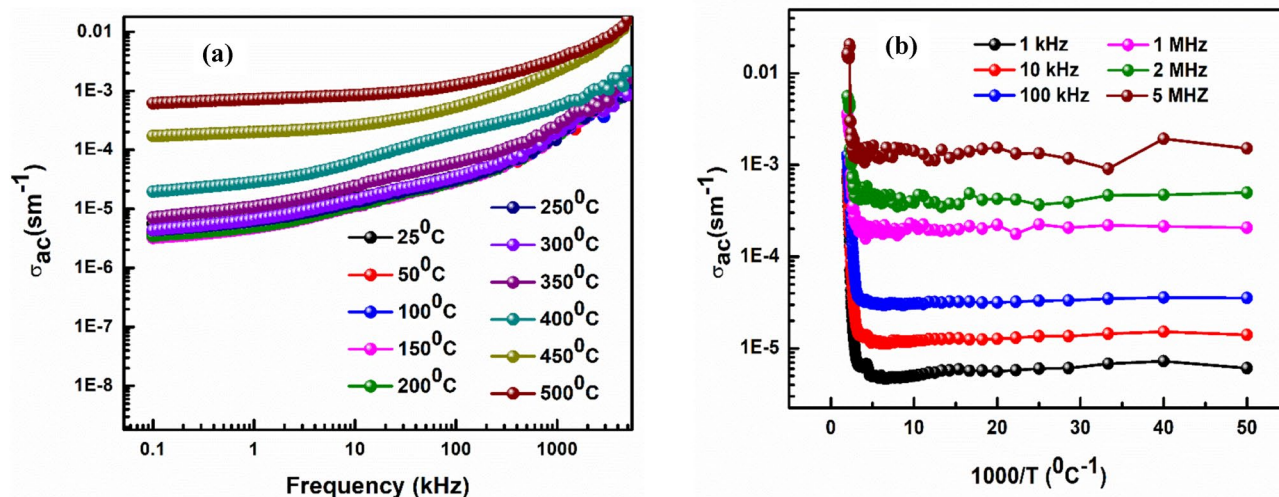
Fig. 8 **a** AC conductivity versus frequency and **b** ac conductivity versus temperature

R = exp(β/T). The linear curve of the lnR versus β as shown in Fig. 9c provides many applications including temperature sensors, medicine, high-temperature thermistor, etc.

3.4 Temperature Coefficient of Resistance

The sensitivity index (α) can be calculated by from Steinhart–Hart coefficient relation as; $\beta = \sqrt{\left(\frac{b}{3c}\right)^3 + \frac{\alpha^2}{4}}$, which can reduce to $\alpha = -\beta/T^2$ [41]. The values of the α are given as; − 0.0216, − 0.0416, − 0.0468, and − 0.0572 at 350 °C, 400 °C, 450 °C and 500 °C respectively. The activation energy (E_a) and sensitivity index (α) can be used to explain the sensitivity of the NTC thermistor. The value of the activation energy can be calculated using a relation; $E_a = k_B$ x β. So, the calculated values of the activation energy are 228 meV, 574 meV, 819 meV and 1234 meV at 350 °C, 400 °C, 450 °C and 500 °C respectively. The presence of variations in the sensitivity index may be due to the extrinsic charge carriers in grains. The stability factor can be defined as the logarithm ratio of the highest value of the resistance to the lowest value of resistance. The stability factor of the sample is 4.45, based on the observed value, it may conclude that the material under study may have excellent NTC thermistor properties.

3.5 Raman Study

Figure 10 represents the Raman spectra of the tetragonal sample. Raman study is one of the sensitive and powerful techniques to analyse order–disorder, local distortion, and short-range symmetry. Again, the determination of the symmetry structure and metal–oxygen stretching modes can also find out from the analysis of Raman spectra. The

active Raman modes of vibrations are observed at 68, 261, 528, and 789 cm^{-1}. The observed broader asymmetric peaks attributed to the TiO_6 octahedra in the solid-state solution.

The presence of A_{1g} symmetry is attributed to the Raman shift at 68 cm^{-1}, which is assigned for oxygen octahedra rotations. The B_{1g} symmetry is confirmed due to the presence of active Raman shift at 528 cm^{-1}, which is assigned to Jahn–Teller-like distortions of oxygen octahedra. Lastly, A_{2g} symmetry is confirmed due to the presence of active Raman shift at 789 cm^{-1}, which is assigned to oxygen octahedra breathing mode [42]. Therefore, the presence of A_{1g}, B_{1g}, and A_{2g} symmetries confirms the tetragonal phase of the prepared sample and also confirms the presence of all constituents' elements.

3.6 UV Visible Study

The semiconducting properties of the prepared sample are studied from the ultraviolet–visible spectrum as shown in Fig. 11a, b. The absorbance spectrum shows the ultraviolet range 306–360 nm; in which the material absorbs the incident radiation more effectively. The cut-off wavelength of the incident radiation in the absorbance spectrum is 350 nm. The energy bandgap of the material is calculated by using Mott and Davis's relation; $\alpha h\nu = A\left(h\nu - E_g\right)^n$, which is equal to 1.67 eV [43]. The calculated bandgap is suitable for photovoltaic applications.

4 Conclusion

The structural analysis of a conventional solid-state reaction method prepared sample suggests a tetragonal crystal structure with space group P4bm. The average crystallite
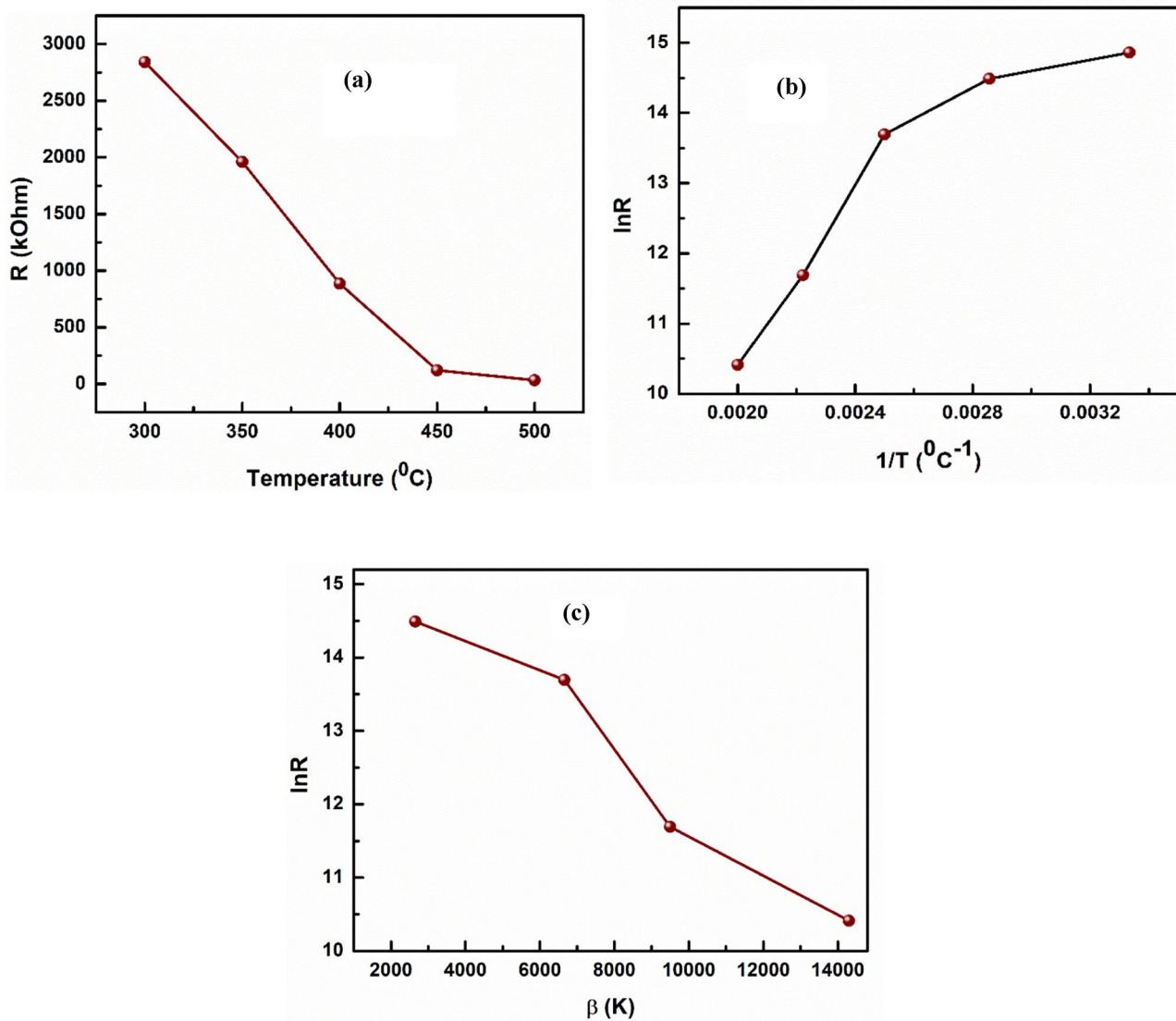
Fig. 9 **a** Resistance versus temperature and **b** lnR versus 1/T, **c** variation of logarithmic of resistance with β(K)
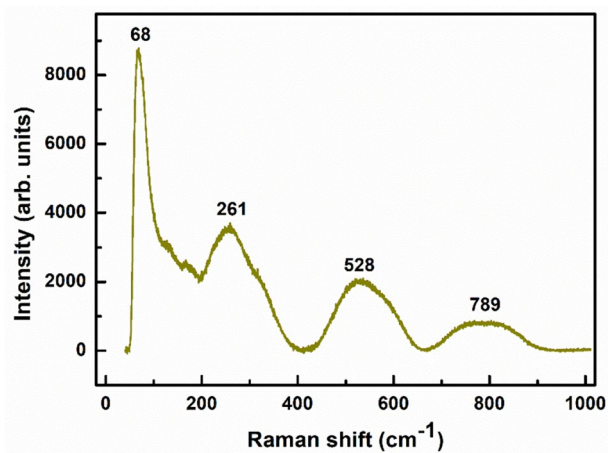

Fig. 10 RAMAN spectrum

size and macrostrain of the sample are 87.2 nm and 0.116% respectively. The sample has an NTCR character explained by dielectric spectroscopy. Non–Debye relaxation process and semiconducting nature of the sample were explained by impedance spectroscopy. The study of ac conductivity reveals the presence of a thermally activated relaxation process. The study of Raman lines confirms the presence of all constituent atomic vibrations. The analysis of the UV visible spectrum of the sample provides the energy bandgap of the 1.67 eV, which is suitable for photovoltaic applications.
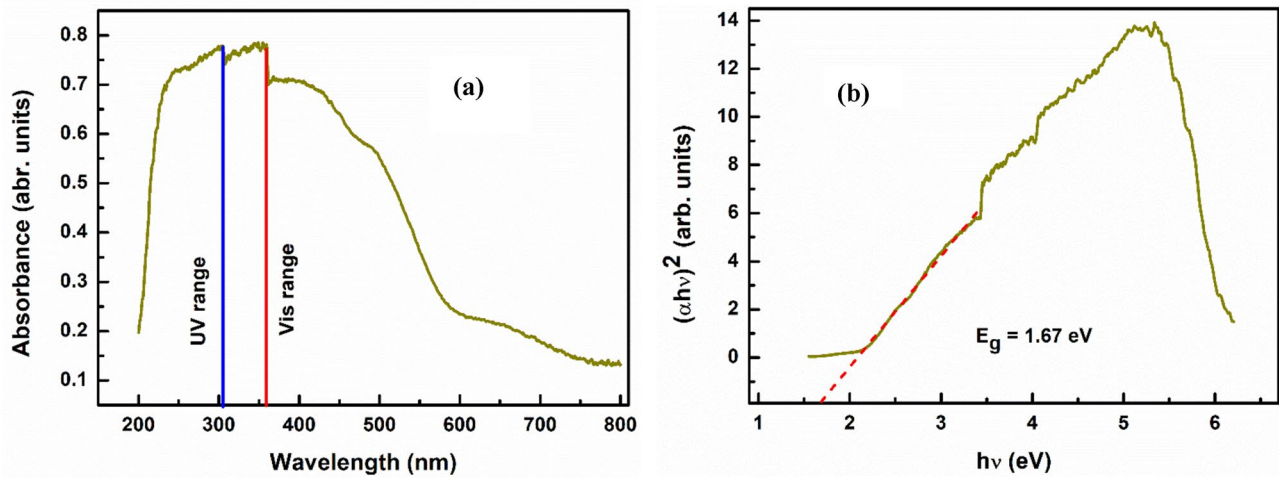
Fig. 11 **a** Absorbance versus wavelength, **b** hν versus $(\alpha h\nu)^2$

Declarations

Conflict of interest There is no conflict of interest as declared by the author.

References

1. F. Jona, G. Shirane, *Ferroelectric Crystals* (MacMillan, New York, 1962)
2. A.P. Alivisatos, Semiconductor clusters nanocrystals, and quantum dots. Science **271**, 933–937 (1996)
3. I.V. Solovyev, K. Terakura, Spin canting in three-dimensional perovskite manganites. Phys. Rev. B. **63**, 174425–174432 (2001)
4. R. Migoni, H. Bilz, D. Bauerle, Origin of Raman scattering and ferroelectricity in oxidic perovskite. Phys. Rev. Lett. **37**, 1155–1158 (1976)
5. V. Garcia, S. Fusil, K.S. Bouzehouane, N.D. Mathur, A. Barthelemy, M. Bibes, Giant tunnel electroresistance for non-destructive readout of ferroelectric states. Nature **460**, 81–84 (2009)
6. J.C. Loudon, N.D. Mathur, P.A. Midgley, Charge-ordered ferromagnetic phase in La$_{0.5}$ Ca$_{0.5}$MnO$_3$. Nature **420**, 797–800 (2002)
7. J.Z. Sun, D.W. Abraham, R.A. Rao, C.B. Eom, Thickness-dependent magneto-transport in ultrathin manganite films. Appl. Phys. Lett. **74**, 3017–3019 (1999)
8. M.N. Rahman, R. Manalert, Grain boundary mobility of BaTiO$_3$ doped with aliovalent cations. J. Eur. Ceram. Soc. **18**, 1063–1071 (1998)
9. A. Biswas, S. Chandra, M.H. Phan, H. Srikanth, Magnetocaloric properties of nanocrystalline LaMnO$_3$: enhancement of refrigerant capacity and relative cooling power. J. Alloys. Compd. **545**, 157–161 (2012)
10. A. Selmi, R. M'nassri, W.C. Koubaa, N.C. Boudjada, A. Cheikhouhou, Influence of transition metal doping (Fe Co, Ni, and Cr) on magnetic and magnetocaloric properties of Pr$_{0.7}$Ca$_{0.3}$Mn$_{O.3}$ manganites. Ceram. Int. **41**, 10177–10184 (2015)
11. B.H. Park, S.J. Hyun, S.D. Bu, T.W. Noh, J. Lee, H.D. Kim, T.H. Kim, W. Jo, Differences in nature of defects between SrBi$_2$Ta$_2$O$_9$ and Bi$_4$Ti$_3$O$_{12}$. Appl. Phys. Lett. **74**, 1907 (1999)
12. J.-C. Yang, Q. He, P. Yu, Y.-H. The Chu, BiFeO$_3$ thin films: a playground for exploring electric-field control of multifunctionalities. Annu. Rev. Mater. Res. **45**, 249–275 (2015)
13. M. Kumar, S. Shankar, R.K. Kotnala, O. Parkash, Evidence of magneto-electric coupling in BFO–BT solid solutions. J. Alloys Compd. **577**, 222–227 (2013)
14. J.-G. Park, M.D. Le, J. Jeong, S. Lee, Structure and spin dynamics of multiferroic BiFeO$_3$. J. Phys. Condens. Matter. **26**, 433202 (2014)
15. K.Y. Yun, D. Ricinschi, T. Kawashima, M. Noda, M. Okuyama, Giant ferroelectric polarization beyond 150 μC/cm^2 in BiFeO$_3$ thin film. Jpn. J. Appl. Phys. **43**, L647–L648 (2004)
16. H.T. Yi, T. Choi, S.G. Choi, Y.S. Oh, S.-W. Cheong, Mechanism of the switchable photovoltaic effect in ferroelectric BiFeO$_3$. Adv. Mater. **23**, 3403–3407 (2011)
17. J. Wang, Epitaxial BiFeO$_3$ multiferroic thin film heterostructures. Science **80**(299), 1719–1722 (2003)
18. S. Sharma, V. Singh, R.K. Kotnala, R.K. Dwivedi, Comparative studies of pure BiFeO$_3$ prepared by sol-gel versus conventional solid-state-reaction method. J. Mater. Sci. Mater. Electron. **25**, 1915–1921 (2014)
19. T. Wang, T. Xu, S. Gao, S.-H. Song, Effect of Nd and Nb co-doping on the structural, magnetic, and optical properties of multiferroic BiFeO$_3$ nanoparticles prepared by sol-gel method. Ceram. Int. **43**, 4489–4495 (2017)
20. K. Chakrabarti, K. Das, B. Sarkar, S.K. De, Magnetic and dielectric properties of Eu-doped BiFeO$_3$ nanoparticles by acetic acid-assisted sol-gel method. J. Appl. Phys. **110**, 103905 (2011)
21. A.R. Makhdoom, M.J. Akhtar, M.A. Rafiq, M.M. Hassan, Investigation of transport behavior in Ba doped BiFe0$_3$. Ceram. Int. **38**, 3829–3834 (2012)
22. Z. Cheng, X. Wang, S. Dou, H. Kimura, K. Ozawa, Improved ferroelectric properties in multiferroic BiFeO$_3$ thin films through La and Nb co-doping. Phys. Rev. B **77**, 092101 (2008)
23. M. Shami, M. Awan, M. Anis-ur-Rehman, Effect of sintering temperature on nanostructured multiferroic BiFeO$_3$ ceramics. Key Eng. Mater. **510**, 348–355 (2012)
24. Y. Saito, H. Takao, T. Tani, T. Nonoyama, K. Takatori, T. Homma, T. Nagaya, M. Nakamura, Lead-free piezoceramics. Nature **432**, 84–87 (2004)
25. K. Mishra, A. Satya, A. Bharathi, V. Sivasubramanian, V. Murthy, A. Arora, Vibrational, magnetic, and dielectric behavior of La-substituted BiFeO$_3$–PbTiO$_3$. J. Appl. Phys. **110**, 123529 (2011)
26. R. Rai, I. Bdikin, M.A. Valente, A.L. Kholkin, Ferroelectric and ferromagnetic properties of Gd-doped BiFe)-3BaTi)$_3$ solid solution. Mater. Chem. Phys. **119**, 539–545 (2010)

🍦 Springer

27 R.J.H. Voorhoeve, *Advanced Materials in Catalysis* (Acadamic Press, London, 1977), p. 129

28. R.I. Hines, in *Atomistic Simulation and Ab-Initio Studies of Polar Solids*. Ph.d., Bristol (1997).

29. R.D. Shannon, Revised effective ionic radii and systematic studies of interatomic distances in halides and chalcogenides. Acta Crystallogr. A **A32**, 751–767 (1976)

30. S.K. Parida, M.K. Swain, R.K. Bhuyan, B. Kisan, R.N.P. Choudhary, Effect of cerium on structural and dielectric properties of the modified $BiFeO_3$–$PbTiO_3$ ceramics for photovoltaic applications. J. Electron. Mater. **50**, 4685–4695 (2021)

31. S.K. Parida, Studies on structural, dielectric, and optical properties of Cu/W double substituted calcium manganite for solar cells and thermistor applications. Phase Transit. **94**, 1033–1052 (2021)

32. S.K. Parida, Structural, electrical and optical properties of zinc and tungsten modified lead titanate ceramics. SPIN **11**, 2150018–2150114 (2021)

33. P.R. Pansara, P.Y. Raval, N.H. Vasoya, S.N. Dolia, K.B. Modi, Intriguing structural and magnetic properties correlation study on Fe^{3+} substituted calcium-copper-titanate. Phys Chem. Chem. Phys. **20**, 1914–1922 (2018)

34. P.G.R. Achary, A.A. Nayak, R.K. Bhuyan, R.N.P. Choudhary, S.K. Parida, Effect of cerium dopant on the structural and electrical properties of $SrMnO_3$ single perovskite. J. Mol. Struct. **1226**, 129391–129399 (2021)

35. S.K. Parida, R.N.P. Choudhary, Preparation method and cerium dopant effects on the properties of $BaMnO_3$ single perovskite. Phase Transit. **93**(10–11), 981–991 (2020)

36. A. Khlifi, R. Hanen, A. Mleiki, H. Rahmouni, N. Guermazi, K. Khirouni, A. Cheikhrouhou, Investigations of electrical properties of $Pr_{0.65}Ca_{0.25}Cd_{0.1}MnO_3$ ceramic. Eur. Phys. J. Plus **135**, 790–794 (2020)

37 P. Ganga Raju Achary, R.N.P. Choudhary, S.K. Parida, Investigation of structural and dielectric properties in polycrystalline $PbMg_{1/3}Ti_{1/3}W_{1/3}O_3$ tungsten perovskite. SPIN **10**(3), 2050021–2050110 (2020)

38. Q. Ke, X. Lou, Y. Wang, J. Wang, Oxygen-vacancy-related relaxation and scaling behaviors of $Bi_{0.9}La_{0.1}Fe_{0.98}Mg_{0.02}O_3$ ferroelectric thin film. Phys. Rev. B Condens. Matter Mater. Phys **82**, 024102–024107 (2010)

39. C. Zhao, B. Wang, P. Yang, L. Winnubst, C. Chen, Effects of Cu and Zn Co-doping on the electrical properties of $Ni_{0.5}Mn_{2.5}O_4$ NTC ceramics. J. Eur. Ceram. Soc. **28**, 35–40 (2008)

40. W. Cao, R. Gerhardt, Calculation of various relaxation times and conductivity for a single dielectric relaxation process. Solid State Ionics **42**, 213–221 (1990)

41. R.N. Jadhav, S.N. Mathad, V. Puri, Studies on the properties of $Ni_{0.6}Cu_{0.4}Mn_2O_4$ NTC ceramic due to Fe doping. Ceram. Int. **38**, 5181–5188 (2012)

42. C. Toulouse, D. Amoroso, C. Xin, P. Veber, M.C. Hatnean, G. Balakrishnan, M. Maglione, P. Ghosez, J. Kreisel, M. Guennou, Lattice dynamics and Raman spectrum of $BaZrO_3$ single crystals. Phys. Rev. B **100**, 134102–134105 (2019)

43. A. Kumar, R. Kumar, N. Verma, A.V. Anupama, H.K. Choudhary, R. Philip, B. Sahoo, Effect of the bandgap and the defect states present within bandgap on the non-linear optical absorption behavior of yttrium aluminum iron garnets. Opt. Mater. **108**, 110163 (2020)